Imaging Based on Communication-Assisted Sensing for UAV-Enabled ISAC

Yunbo Hu⋆†, Liang Tang⋆, Xiaoxiao Zhuo⋆, Zhanya Li⋆, Wen Wu‡, Yu Zhao⋆ and Zhiyong Bu⋆
⋆Shanghai Institute of Microsystem and Information Technology, Chinese Academy of Sciences, Shanghai 200050, China
†University of Chinese Academy of Sciences, Beijing 101408, China
‡Frontier Research Center, Peng Cheng Laboratory, Shenzhen 518055, China
Email: {huyb, liang.tang, zhuoxx, zhanya.li, yu.zhao, zhiyong.bu}@mail.sim.ac.cn⋆, wuw02@pcl.ac.cn‡

***Abstract*—In this paper, we propose an imaging scheme for unmanned aerial vehicle (UAV)-Enabled integrated sensing and communication (ISAC), where the UAV serves as a flexible communication auxiliary and a versatile sensing platform with the cooperation of a ground base station (GBS). To guarantee the performance of both sensing and communication, the proposed imaging scheme is based on the orthogonal frequency division modulation (OFDM) ISAC waveform and bistatic communication-assisted sensing strategy, which can be divided into three steps. Firstly, the UAV transmits OFDM ISAC signal, which contains the UAV position information to enable the communication-assisted sensing strategy. Secondly, the GBS receives the line-of-sight (LoS) ISAC signal from the UAV and the reflected ISAC signal from targets, in which the bistatic sensing architecture is designed to process data frequently and bypass the self-interference problem. Thirdly, the GBS preprocesses the received signal and reconstructs the image based on polar format algorithm (PFA) with the knowledge of UAV positions to relax the constraint of UAV trajectory. Numerical simulations are carried out to validate and evaluate the proposed UAV-enabled ISAC imaging scheme.**

I. Introduction

Integrated sensing and communication (ISAC) has emerged as a promising technology for the future wireless communication framework, in which radar sensing and wireless communication share the waveform and hardware for higher spectrum efficiency [1], [2]. Unmanned aerial vehicle (UAV)-assisted sensing is widely applied for aerial photographing, surveying, and mapping. Synthetic aperture radar (SAR) is a typical imaging technology, which benefits from all-weather monitoring. UAV-enabled communication can increase the communication coverage and capacity with the feature of flexibility to optimize the communication channel [3], [4]. Thus, UAV is a promising platform for future ISAC applications.

The study of UAV-enabled ISAC-based imaging is still in its early stage and faces some challenges. Firstly, the existing works are mainly focused on the *monostatic* sensing framework. A joint communication and SAR waveform design is proposed in [5] based on a modified Alamouti coding scheme to integrate sensing waveform into OFDM communication waveform. The OFDM-based SAR imaging scheme is first studied in [6]. However, the sensing data cannot be accessed frequently on the ground in the monostatic framework, resulting from the large computational and transmission cost for lightweight UAVs. Meanwhile, the communication-centric waveform design in the monostatic framework suffers from severe self-interference or low duty cycle. Secondly, the *flexible trajectory* design in UAV-enabled communication seems to conflict with the predetermined trajectory design in UAV sensing. [7] and [8] design the trajectory of UAVs considering both the sensing performance and communication performance. However, no efficient sensing method is provided in these works. Different from the existing works, this paper proposes the bistatic communication-assisted sensing strategy to tackle the above challenges.

In this paper, we propose a novel UAV-enabled ISAC imaging scheme with the cooperation of a ground base station (GBS), similar to airborne/stationary SAR, together with a three-stage bistatic communication-assisted sensing strategy. Firstly, UAV transmits OFDM-based ISAC signal conveying position information. Secondly, the GBS receives line-of-sight (LoS) ISAC signal from the UAV and the reflected signal from targets. The bistatic design features frequent monitoring as the receiver is stationary on the ground [9] and bypasses the problem of self-interference as the transmitter (Tx) and sensing receiver (Rx) are separated. Therefore, the communication functions can remain unaffected as much as possible. Thirdly, the GBS synchronizes the signal and preprocesses the data with the knowledge of UAV positions. The preprocessing includes phase compensation and interpolation grid determination. Accordingly, the image can be reconstructed based on the polar format algorithm (PFA). To validate and evaluate the proposed UAV-enabled ISAC imaging scheme, a numerical simulation experiment is carried out under two specific conditions: a classical fixed straight-line trajectory and a communication-optimized trajectory.

Thus, our contributions are summarized as follows:

- We design a novel imaging scheme for UAV-enabled ISAC that can achieve timely processing and acquisition of data, and bypass the self-interference problem.
- We propose a bistatic communication-assisted sensing strategy for the imaging scheme, which preserves the flexibility of UAV trajectory.

The remainder of this paper is organized as follows. The sytem model of the proposed UAV-enabled ISAC imaging scheme is presented in Section II. Section III describes the proposed communication-assisted sensing strategy. Simulation results are given in Section IV, along with the conclusion in Section V.

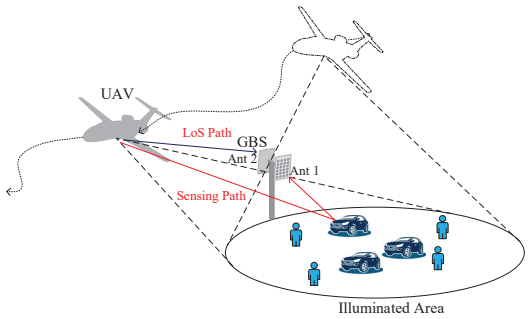

Fig. 1. Basic framework of UAV-enabled ISAC imaging.

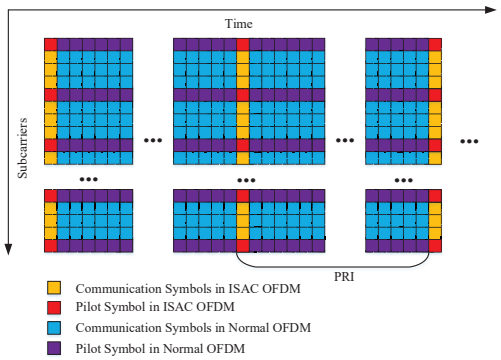

Fig. 2. An illustration of OFDM subcarrier allocation.

II. System Model

A. System Framework

As illustrated in Fig. 1, the UAV-enabled ISAC imaging framework consists of a UAV, a GBS, several user equipments (UEs), and several targets. The system framework can perform both sensing and communication functions.

In the sensing scenario, the UAV works as the Tx of a spotlight airborne/stationary SAR and transmits the OFDM ISAC signal, and it is configured to keep the beam illuminating the same area. The trajectory of the UAV is not certain and can be flexibly designed. The GBS is equipped with two antenna arrays, namely Ant1 and Ant2 as shown in Fig. 1. As such, the Ant1 can receive the reflected sensing signal from the targets for sensing and the Ant2 can receive the LoS ISAC signal for LoS interference mitigation and synchronization. Suppose that the LoS interference mitigation is sufficient, the LoS interference is ignored in the rest of the paper. Note that the raw data can be immediately processed on the GBS without waiting for the UAV to land, which means that the imaging results can be obtained in a more frequent and timely manner.

In the communication scenario, UAV performs as a temporary base station or relay node, transmitting downlink ISAC signal to GBS and UEs in the illuminated area. GBS receives and demodulates the ISAC signal to obtain the embedded position information of the UAV. When UAV is not sensing or not in charge of the communication of the area, GBS can also perform as the communication BS to serve UEs.

B. Signal Model

The ISAC signal is designed to perform both sensing and communication functions. In this paper, we apply the OFDM waveform as the ISAC signal, where the communication symbols and pilots are placed in different subcarriers. Since the randomness of communication symbols would affect the sensing result [5], only the dedicated Zadoff-Chu sequence pilot is adopted for sensing. With M subcarriers configured, the n-th transmitted OFDM signal $s_n(t)$ can be written as

$$s_n(t) = \sum_{m=0}^{M-1} S_{m,n} \exp\left[j2\pi f_m(t - nT_s)\right] \mathrm{Rect}(t - nT_s), \tag{1}$$

where $S_{m,n}$ denotes the symbol in the m-th subcarrier of the n-th OFDM symbol, $f_m = f_c + m\Delta f$ denotes the m-th subcarrier frequency, f_c denotes the carrier frequency, Δf is the subcarrier interval, $T_{\mathrm{s}} = 1/\Delta f + T_{CP}$ denotes the duration of the OFDM symbol which consists of the cyclic prefix (CP) duration T_{CP} and the OFDM elementary duration $1/\Delta f$, and $\mathrm{Rect}(t)$ is the rectangle window function with value 1 only in $[-T_{CP}, \frac{1}{\Delta f}]$.

As illustrated in Fig. 2, the transmitted OFDM symbol can be classified into two types, namely, the ISAC OFDM symbol and the normal OFDM symbol. The time interval between two successive ISAC OFDM symbols is denoted as the pulse repetition interval (PRI). The PRI of ISAC OFDM should be delicately designed since it will affect wavenumber spectrum interpolation, therefore, affect the image reconstruction. And the pilot symbols are placed in Comb-4 style. Thus, the transmitted symbols satisfy

$$S_{m,n} = \begin{cases} C_{m-\lceil m/4 \rceil, n}, & m \mod 4 \neq 0, \\ P_{m/4}, & m \mod 4 = 0, \end{cases} \tag{2}$$

where $C_{m-\lceil m/4 \rceil, n}$ denotes the $m - \lceil m/4 \rceil$-th communication symbol in the n-th OFDM block and $P_{m/4}$ denotes the $m/4$-th pilot symbol.

Since the ISAC OFDM waveform is designed with the communication-centric principle, the communication function of the system can be unchanged. Thus, in the following part of the paper, we only focus on the sensing function of the system. Under the assumption of a single point target, the received sensing signal of GBS can be modeled as a time shift version of (1):

$$s_{r,n}(t) = \sigma(x,y,z) \sum_{m=0}^{M-1} S_{m,n} \exp[j2\pi f_m(t - nT_P - \frac{R_n}{c})] \mathrm{Rect}(t - nT_P - \frac{R_n}{c}) + z_n(t), \tag{3}$$

$$s_{s,n}(t) = h \sum_{m=0}^{M-1} S_{m,n} \exp[j2\pi f_m(t - nT_P - \frac{R_{LoS,n}}{c})] \mathrm{Rect}(t - nT_P - \frac{R_{LoS,n}}{c}) + z_{S,n}(t). \tag{4}$$

Here, $s_{r,n}(t)$ and $s_{s,n}(t)$ denote the n-th received reflected ISAC OFDM signal and LoS ISAC OFDM signal, respectively. $\sigma(x,y,z) \in \mathbb{C}$ denotes the radar cross section (RCS) of the target located at (x,y,z), which is assumed to be constant.

$h \in \mathbb{C}$ is the amplitude of LoS signal. c denotes the speed of light. $z_n(t)$ and $z_{S,n}(t)$ denote the received Gaussian white noise with spectral density N_0. R_n and $R_{LoS,n}$ are the range of the reflected path and LoS path, which are denoted by

$$R_n = \|\vec{r}_n - \vec{r}\| + \|\vec{r} - \vec{r}_G\|, \tag{5}$$

$$R_{LoS,n} = \|\vec{r}_n - \vec{r}_G\|, \tag{6}$$

where the vectors $\vec{r}_n = (x_n, y_n.z_n)$, $\vec{r}_G = (x_G, y_G, z_G)$, and $\vec{r} = (x, y, z)$ denote the location of the UAV, the location of the GBS, and the location of the target at the n-th sensing moment, respectively. The origin of the coordinate is defined as the center of the illuminated area. Actually, path loss should be considered in RCS [7], namely $\sigma(x, y, z) = \frac{\beta_0 E_t \sigma_0}{\|\vec{r}_n - \vec{r}\| \|\vec{r} - \vec{r}_G\|}$, where β_0 denotes the sensing path loss parameter, E_t is the average transmit power and σ_0 denotes the real RCS.

III. Communication-Assisted Sensing Based Imaging Algorithm

A. Communication Assisted Sensing Signal Synchronization

To demodulate the received sensing signal at GBS, the signal should be synchronized between the transmitted signal and the received signal. However, the GBS and UAV cannot keep synchronized due to the separation. In this paper, we propose a communication-assisted sensing signal synchronization method to alleviate the inevitable clock deviation between GBS and UAV. After the removal of CP, OFDM demodulation, and extraction of the pilot symbols, the received sensing signal can be modeled into the matrix format, i.e.,

$$\begin{aligned}\mathbf{P}_{l,n} =& \sigma(x, y, z) P_l \exp[-j2\pi(f_c + 4l\Delta f)(R_n/c + \Delta_{\tau,n})] \\ =& \sigma(x, y, z) P_l \exp[-jk_l(R_n + \Delta_{R,n})] + \omega_{l,n},\end{aligned} \tag{7}$$

$$\begin{aligned}\mathbf{P}^S_{l,n} =& hP_l \exp[-j2\pi(f_c + 4l\Delta f)(R_{LoS,n}/c + \Delta_{\tau,n}) \\ =& hP_l \exp[-jk_l(R_{LoS,n} + \Delta_{R,n})] + \omega^S_{l,n},\end{aligned} \tag{8}$$

where $\mathbf{P}_{l,n}$ and $\mathbf{P}^S_{l,n}$ denote the element at the l-th row and the n-th column of the reflected pilot matrix and LoS matrix, $l = 0, 1, \ldots, \lfloor M/4 \rfloor$ is the index of pilots, $k_l = 2\pi(f_c + 4l\Delta f)/c$ denotes the wavenumber of the l-th pilot subcarrier, $\Delta_{\tau,n}$ denotes the clock deviation which is different at different OFDM symbols, $\Delta_{R,n}$ is defined as $\Delta_{R,n} = c\Delta_{\tau,n}$, and $\omega_{l,n}$ and $\omega^S_{l,n}$ denote the noise after sampling and demodulation with an average power of $M\Delta f N_0$. For simplicity, the effect of noise is ignored in the following theoretical part. It is worth noting that in the proposed sensing the CP length needs to be longer than the maximal delay between the reflected signal and the LOS signal to avoid inter-subcarrier interference.

Despite the uncertainty of $\Delta_{\tau,n}$, since the time deviations are the same in $\mathbf{P}_{l,n}$ and $\mathbf{P}^S_{l,n}$, it can be eliminated by elementary conjugate multiplication, which can be denoted by

$$\begin{aligned}\tilde{\mathbf{P}}_{l,n} &= \mathbf{P}_{l,n} \times \mathrm{conj}(\mathbf{P}^S_{l,n}) \\ &= \tilde{\sigma}(x, y, z) \exp[-jk_l(R_n - R_{LoS,n})],\end{aligned} \tag{9}$$

where $\tilde{\sigma}(x, y, z)$ is the effective RCS and defined as $\tilde{\sigma}(x, y, z) = \sigma(x, y, z)h^*$. From (9), the $\tilde{\mathbf{P}}$ is still affected by $R_{LoS,n}$. Furthermore, the position of the UAV is conveyed in the ISAC OFDM communication signal and the position of GBS is known in advance. As a result, $R_{LoS,n}$ can be calculated. Thus the impact of $R_{LoS,n}$ can be mitigated by phase compensation:

$$\begin{aligned}\hat{\mathbf{P}}_{l,n} &= \tilde{\mathbf{P}}_{l,n} \exp(-jk_l R_{LoS,n}) \\ &= \tilde{\sigma}(x, y, z) \exp[-jk_l R_n],\end{aligned} \tag{10}$$

where the UAV position information is assumed to be perfect. As for the imperfect situation, it will be discussed in future work.

B. Communication-Assisted Signal Preprocessing

With the synchronized signal, the next step involves signal preprocessing, which is based on communication-assisted sensing and the principle of PFA. Assuming the UAV and GBS are relatively far from the illuminated area, (5) can be approximated as:

$$\begin{aligned}R_n &\overset{(a)}{\approx} \|\vec{r}_n\| - \frac{\vec{r}_n}{\|\vec{r}_n\|} \cdot \vec{r} + \|\vec{r}_G\| - \frac{\vec{r}_G}{\|\vec{r}_G\|} \cdot \vec{r} \\ &= (\|\vec{r}_n\| + \|\vec{r}_G\|) - (\frac{\vec{r}_n}{\|\vec{r}_n\|} + \frac{\vec{r}_G}{\|\vec{r}_G\|}) \cdot \vec{r},\end{aligned} \tag{11}$$

where (a) is based on the first-order Taylor expansion $\|\vec{r}_0 - \vec{r}\| \approx \vec{r}_0 - \frac{\vec{r}_0}{\|\vec{r}_0\|} \cdot \vec{r}$. The approximation induces more error when $\|\vec{r}\|$ increases or $\|\vec{r}_0\|$ decreases. Assuming the imaging target is on the ground, $\vec{r}$ can be denoted by $\vec{r} = (x, y, 0)$ and $\tilde{\sigma}(x, y, z)$ can be simplified as $\tilde{\sigma}(x, y)$. Define $\vec{\rho}_n = \frac{\vec{r}_n}{\|\vec{r}_n\|} + \frac{\vec{r}_G}{\|\vec{r}_G\|} = (\rho_{x,n}, \rho_{y,n}, \rho_{z,n})$. Thus, (11) can be rewritten as:

$$\begin{aligned}R_n &= (\|\vec{r}_n\| + \|\vec{r}_G\|) - \vec{\rho}_n \cdot \vec{r} \\ &= (\|\vec{r}_n\| + \|\vec{r}_G\|) - x\rho_{x,n} - y\rho_{y,n},\end{aligned} \tag{12}$$

Substituting (12) into (10), we can obtain:

$$\begin{aligned}\hat{\mathbf{P}}_{l,n} =& \tilde{\sigma}(x, y) \exp[-jk_l(\|\vec{r}_n\| + \|\vec{r}_G\| - x\rho_{x,n} - y\rho_{y,n})] \\ =& \tilde{\sigma}(x, y) \exp(jk_l\rho_{x,n}x + jk_l\rho_{y,n}y) \\ & \exp[-jk_l(\|\vec{r}_n\| + \|\vec{r}_G\|)].\end{aligned} \tag{13}$$

Similarly, the second exponential term could also be compensated with position information known in advance. The compensated signal can be written as

$$\begin{aligned}\overline{\mathbf{P}}_{l,n} &= \hat{\mathbf{P}}_{l,n} \exp[jk_l(\|\vec{r}_n\| + \|\vec{r}_G\|)] \\ &= \tilde{\sigma}(x, y) \exp(jk_l\rho_{x,n}x + jk_l\rho_{y,n}y).\end{aligned} \tag{14}$$

The above analysis is based on a single point target, as for more general extended targets, due to the linearity, (14) can be rewritten in an integration form

$$\overline{\mathbf{P}}_{l,n} = \iint \tilde{\sigma}(x, y) \exp(jk_l\rho_{x,n}x + jk_l\rho_{y,n}y) dxdy. \tag{15}$$

From (15), it is clear that $\overline{\mathbf{P}}_{l,n}$ equals to a sample of $\tilde{\sigma}(x, y)$'s 2-D inverse Fourier transform $F_{\tilde{\sigma}}$, namely

$$\overline{\mathbf{P}}_{l,n} = F_{\tilde{\sigma}}(k_x, k_y)|_{k_x = k_l\rho_{x,n}, k_y = k_l\rho_{y,n}}, \tag{16}$$

where the k_x and k_y denote the wavenumber along x-axis and y-axis.

With completed wavenumber spectrum information, the image can be reconstructed via Fourier Transform. Nevertheless,

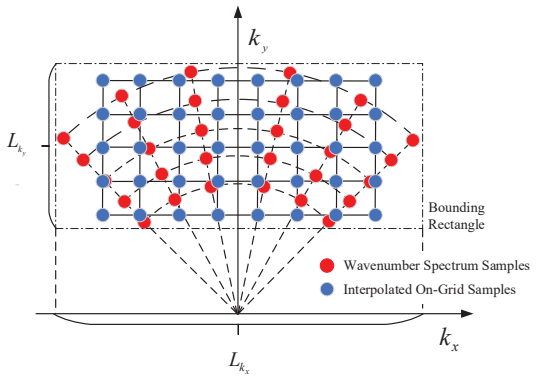

Fig. 3. Illustration of wavenumber spectrum samples and on-grid interpolation.

the samples are not continuous in the wavenumber spectrum. Fig.3 illustrates the position of wavenumber samples in the wavenumber domain. From (16), it is clear that samples obtained from the same OFDM symbol are uniformly located on a line passing through the origin. However, samples should be located uniformly on the grid like the blue dots in Fig. 3, to adopt 2-dimensional discrete Fourier transform (2D-DFT) for imaging. As the grid cannot be boundless, it should be determined before interpolation. To ensure interpolation accuracy, the range of the grid should overlap with the range of the samples as much as possible. However, due to the arbitrariness of the UAV trajectory in our proposed scheme, the positions of samples are not certain, resulting in the uncertainty of the grid point position.

To solve this problem, an adaptive interpolation grid determination method is proposed. First, find the maximum and minimum of k_x and k_y of the samples and denote them as $k_{x,\max}$, $k_{x,\min}$, $k_{y,\max}$ and $k_{y,\min}$, respectively. These maximums/minimums can determine a rectangular area of the wavenumber spectrum. As shown in Fig. 3 the sample area is bounded in the rectangle. Similar to the relationship between time and frequency, the interval of the grid satisfies

$$\Delta k_x = \frac{\pi}{x_{\max}}, \tag{17}$$

$$\Delta k_y = \frac{\pi}{y_{\max}}, \tag{18}$$

where $x_{\max}$ and $y_{\max}$ are the maximum coordinate value of the image, as the pixels satisfy $x \in [-x_{\max}, x_{\max}]$ and $y \in [-y_{\max}, y_{\max}]$. With the determined wavenumber interval Δk_x and Δk_y and the bounding rectangle, the uniformly positioned grid point $k_{x,i}, k_{y,j}$ can be calculated as follows

$$k_{x,p} = k_{x,c} + p\Delta k_x, \tag{19}$$

$$k_{y,q} = k_{y,c} + q\Delta k_y. \tag{20}$$

In (19) and (20), $(k_{x,c}, k_{y,c})$ denotes the center of the bounding rectangle, which satisfies $k_{x,c} = (k_{x,\max} + k_{x,\min})/2$ and $k_{y,c} = (k_{y,\max} + k_{y,\min})/2$, and the indices p, q satisfy $p = -P/2, \ldots, 0, P/2-1$ and $q = -Q/2, \ldots, 0, Q/2-1$, where P, Q are two even numbers and they should satisfy that the grid span $I\Delta k_x$ and $J\Delta k_y$ is close to the bounding box side lengths $L_{k_x} = k_{x,\max} - k_{x,\min}$ and $L_{k_y} = k_{y,\max} - k_{y,\min}$ respectively.

C. Image Reconstruction

After the preprocessing and the determination of the grid, the PFA-based interpolation can be then executed. Then, 2D-DFT can be used to reconstruct the image. Assuming the interpolation is perfect, the 2D-DFT result of a single point target located at (x_0, y_0) can be expressed as

$$\begin{aligned} I(\tilde{p}, \tilde{q}) &= \mathrm{2DDFT}[F_{\tilde{\sigma}}(k_{x,p}, k_{y,q})] \\ &\overset{(b)}{=} \sum_{p=-\frac{P}{2}}^{\frac{P}{2}-1} \sum_{q=-\frac{Q}{2}}^{\frac{Q}{2}-1} \tilde{\sigma}(x_0, y_0) \exp(jk_{x,c}x_0 + jk_{y,c}y_0) \\ &\qquad \exp[-jp\Delta k_x(x - x_0) - jq\Delta k_y(y - y0)] \\ &= \tilde{\sigma}(x_0, y_0) \exp(jk_{x,c}x_0 + jk_{y,c}y_0) \\ &\qquad G_x(\tilde{p}\Delta_x - x_0) G_y(\tilde{q}\Delta_y - y_0), \end{aligned} \tag{21}$$

where $\tilde{p} = -P/2, \ldots, 0, P/2-1, \tilde{q} = -Q/2, \ldots, 0, Q/2-1$ denote the indices of the image pixel. The relation between the indices and the position is $x = \tilde{p}\Delta x, y = \tilde{q}\Delta y$. Δx and Δy means the pixel resolutions. The equation (b) is based on (17) and (18). And the point spread functions $G_x(x), G_y(y)$ are defined as

$$G_x(x) = \frac{\sin(\frac{1}{2}P\Delta k_x x)}{\sin(\frac{1}{2}\Delta k_x x)} \exp(-j\frac{1}{2}\Delta k_x x), \tag{22}$$

$$G_y(x) = \frac{\sin(\frac{1}{2}Q\Delta k_y y)}{\sin(\frac{1}{2}\Delta k_y y)} \exp(-j\frac{1}{2}\Delta k_y y). \tag{23}$$

$G_x(x)$ and $G_y(y)$ peak at $x = 0$ and $y = 0$. Thus, the magnitude image can be represented by $|I(\tilde{p}, \tilde{q})|$. The approximation error in (11) is small in spaceborne sensing, but in UAV sensing, the error would be non-negligible. An off-the-shelf subfigure-based phase compensation method for PFA can be adopted to post-process the image to reduce the reconstruction error. The detail of the method can be referred to in [10]. It is worth noting that, in our proposed flexible scheme, the choice of interpolation, reconstruction, and correction methods is not limited.

IV. Numerical Simulation

Numerical simulation is carried out to validate and evaluate the proposed UAV-enabled ISAC imaging scheme. In the simulation, the carrier frequency is $f_c = 5.8\,\mathrm{GHz}$, the number of subcarriers is $M = 2048$, the pilot is the 25-th root Zadoff-Chu sequence with a length of 511, the subcarrier interval is $\Delta f = 60\,\mathrm{kHz}$, the number of ISAC OFDM for imaging is $N = 800$, and the communication symbols are mapped to 16-QAM symbols. The imaging area is set as $x \in [-25, 25]\,\mathrm{m}, y \in [-25, 25]\,\mathrm{m}$, and the GBS is located at $\vec{r}_G = (0\,\mathrm{m}, -100\,\mathrm{m}, 20\,\mathrm{m})$. We have taken path loss into consideration. The transmit power is 45 dBm, the RCS σ_0 is 1, the noise spectral density is $N_0 = -174\,\mathrm{dBm}$ and the path loss parameter β_0 is $-30\,\mathrm{dB}$. 25 ideal point targets are located at the illuminated area as shown in Fig. 4(a).

We have considered two scenarios. In scenario A, the UAV flies along a straight line from $(-50\,\mathrm{m}, -150\,\mathrm{m}, 50\,\mathrm{m})$ to $(50\,\mathrm{m}, -150\,\mathrm{m}, 50\,\mathrm{m})$, which is the commonly applied trajectory for imaging, while in scenario B, the UAV flies

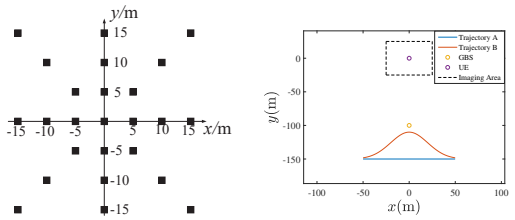

(a) Location of the targets. (b) Trajectories in two scenarios.

Fig. 4. Aerial views of the point targets and the trajectories.

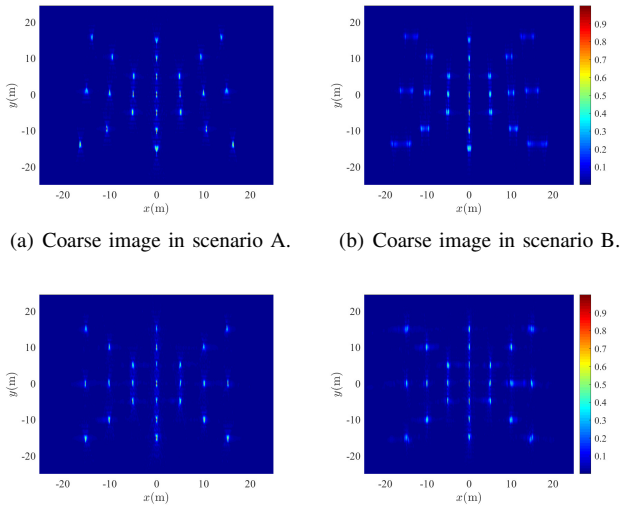

(a) Coarse image in scenario A. (b) Coarse image in scenario B.

(c) Corrected image in scenario A. (d) Corrected image in scenario B.

Fig. 5. Imaging results.

along a curve, which is similar to the communication rate maximizing trajectory in [3]. The aerial view of the trajectory in the scenario A and B is shown in Fig. 4(b). And the imaging performance of the target at $(12.5\,\mathrm{m}, 12.5\,\mathrm{m})$ under different transmit power is further studied.

The normalized imaging result in scenario A is shown in Fig. 5(a). The point targets are focused, but the image is distorted. The targets with longer polar radii and targets closer to the UAV and GBS tend to distort more. It is caused by approximation error in (11). This phenomenon also exists in Scenario B. Moreover, as shown in Fig.5(b), some targets are defocused too severely to be detected as targets. Fig. 5(c) and Fig. 5(d) show the corrected images, which indicates that distortion and defocusing can be resolved to some extent by the adopted post-processing algorithm.

Fig. 6(a) and Fig. 6(b) illustrate the mean squared error (MSE) of the imaging center versus the transmit power. When transmit power is lower than $25\,\mathrm{dBm}$, the image point is covered by noise, leading to high MSE values. As the transmit power exceeds $30\,\mathrm{dBm}$, the MSEs generally converge to a constant value, because of the imperfect correction method. However, this bias is acceptable for positioning. In general, the performance in scenario A is better, so the classical trajectory is more proper for our proposed imaging scheme. Namely, there is a trade-off of trajectory design between better imaging quality and communication performance in our scheme.

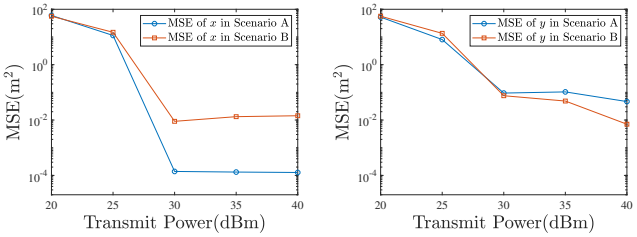

(a) MSE of x. (b) MSE of y.

Fig. 6. MSE of the point target center.

V. Conclusion

We proposed a novel UAV-enabled ISAC imaging scheme. UAV and the GBS cooperate with each other to construct bistatic sensing architecture enabling frequent access and processing of the sensing data and the bistatic design can bypass the self-interference problem. The communication-assisted sensing strategy relaxes the trajectory constraint of the UAV. The preprocessing method containing phase compensation and interpolation grid determination is proposed, and the PFA-based imaging method is adopted to reconstruct the image of targets. The performance of the proposed scheme is provided in terms of the image results and the image MSE. In future work, we will study joint trajectory design and target sensing scheme.

References

[1] F. Liu and C. Masouros, "A Tutorial on Joint Radar and Communication Transmission for Vehicular Networks—Part I: Background and Fundamentals," *IEEE Communications Letters*, vol. 25, no. 2, pp. 322–326, Feb. 2021.

[2] F. Liu, Y. Cui, C. Masouros, *et al.*, "Integrated Sensing and Communications: Toward Dual-Functional Wireless Networks for 6G and Beyond," *IEEE J. Select. Areas Commun.*, vol. 40, no. 6, pp. 1728–1767, Jun. 2022.

[3] Y. Zeng and R. Zhang, "Energy-Efficient UAV Communication With Trajectory Optimization," *IEEE Transactions on Wireless Communications*, vol. 16, no. 6, pp. 3747–3760, Jun. 2017.

[4] J. Mu, R. Zhang, Y. Cui, N. Gao, and X. Jing, "UAV Meets Integrated Sensing and Communication: Challenges and Future Directions," *IEEE Communications Magazine*, vol. 61, no. 5, pp. 62–67, May 2023.

[5] J. Wang, X.-D. Liang, L.-Y. Chen, L.-N. Wang, and K. Li, "First Demonstration of Joint Wireless Communication and High-Resolution SAR Imaging Using Airborne MIMO Radar System," *IEEE Transactions on Geoscience and Remote Sensing*, vol. 57, no. 9, pp. 6619–6632, Sep. 2019.

[6] T. Zhang and X.-G. Xia, "OFDM Synthetic Aperture Radar Imaging With Sufficient Cyclic Prefix," *IEEE Transactions on Geoscience and Remote Sensing*, vol. 53, no. 1, pp. 394–404, Jan. 2015.

[7] X. Jing, F. Liu, C. Masouros, and Y. Zeng, "ISAC from the Sky: UAV Trajectory Design for Joint Communication and Target Localization," *arXiv e-prints*, arXiv:2207.02904, 2022.

[8] A. V. Savkin, W. Ni, and M. Eskandari, "Effective UAV Navigation for Cellular-Assisted Radio Sensing, Imaging, and Tracking," *IEEE Transactions on Vehicular Technology*, pp. 1–6, 2023.

[9] H. Zhang, Y. Deng, R. Wang, *et al.*, "Spaceborne/Stationary Bistatic SAR Imaging With TerraSAR-X as an Illuminator in Staring-Spotlight Mode," *IEEE Transactions on Geoscience and Remote Sensing*, vol. 54, no. 9, pp. 5203–5216, Sep. 2016.

[10] X. Mao, D. Zhu, and Z. Zhu, "Polar Format Algorithm Wavefront Curvature Compensation Under Arbitrary Radar Flight Path," *IEEE Geosci. Remote Sensing Lett.*, vol. 9, no. 3, pp. 526–530, May 2012.